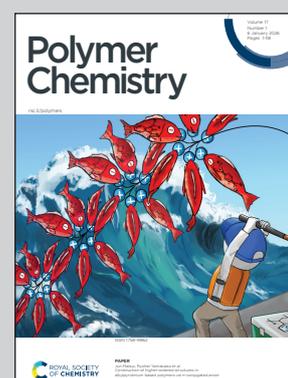**Sequential steps**

Intermediates rearrange

Showcasing research from Professor Dharmapura Murthy's laboratory, Department of Chemistry, Manipal Institute of Technology, Manipal Academy of Higher Education, Manipal, Karnataka, India.

A precursor-dependent distinctive polymerization process controls the optoelectronic properties of graphitic carbon nitride photocatalyst

This work provides mechanistic insights into how changing the precursor impacts the various intermediates formed during the thermal polymerization process of graphitic carbon nitride (g-C_3N_4), a versatile photocatalyst. A comprehensive correlation is established between the polymerization mechanism and the optoelectronic, photophysical, structural, and photoelectrochemical properties of g-C_3N_4. Results aid in tailoring the properties of g-C_3N_4 to enhance solar-to-chemical energy conversion efficiency by controlling the polymerisation process.

Image reproduced by permission of Simon Joyson Galbao and Dharmapura H. K. Murthy from *Polym. Chem.*, 2026, **17**, 35.

ROYAL SOCIETY OF **CHEMISTRY**

Check for updates

A precursor-dependent distinctive polymerization process controls the optoelectronic properties of graphitic carbon nitride photocatalyst

Simon Joyson Galbao, [ID] Sherlin Samantha Menezes, [ID] Syeda Reha Khadri [ID] and Dharmapura H. K. Murthy [ID] *

Due to its metal-free polymeric nature, ease of synthesis using low-cost earth-abundant precursors and tunable optoelectronic properties, graphitic carbon nitride (GCN) is extensively used in solar fuel production. Despite two decades of extensive research, the fundamentals of the thermal polymerization process leading to the formation of GCN are inadequately understood. In this work, we employ cyanamide (CYN) and dicyandiamide (DCDA) precursors and systematically reveal the polymerization mechanism. Though CYN has half the amount of C and N compared with DCDA, it yielded virtually similar structural properties and a similar degree of conjugation that determines the energetic difference for π-to-π^* fundamental (optical) transitions and photoexcited lifetimes. Detailed complementary analysis using thermal methods, along with quantifying the amount of NH_3 released using the temperature-programmed desorption technique, offered unique insights into the polymerization process. Unlike previous notions, the results unambiguously demonstrate that GCN formation need not always release NH_3 as a result of a thermal condensation reaction. Rather, it is possible that molecular rearrangement (dimerization and/or cyclization) of intermediate condensates can also play a major role in the formation of melamine, which is found to be an important intermediate. The obtained mechanistic insights into the thermodynamics of the polymerization process and its impact on optoelectronic properties and photoelectrochemical performance will aid the rational design of GCN to enhance the efficiency of solar energy conversion.

1. Introduction

Among the wide range of semiconductor materials developed recently, graphitic carbon nitride (GCN) has gained significant attention due to its metal-free structure, ease of preparation, chemical stability, and absorption edge in the visible region, especially when compared to extensively used oxide-based photocatalysts.[1] In contrast to metal-based semiconductors that raise concerns related to toxicity, cost and long-term environmental impact, GCN offers a cost-effective alternative photocatalyst with tunable optoelectronic and surface properties. These prospects enable its application in photocatalytic H_2 evolution,[2,3] CO_2 reduction,[4] pollutant degradation[5] and organic transformation reactions.[6,7]

GCN can be easily synthesized *via* thermal condensation using a variety of cost-effective N-rich precursors like cyanamide (CYN),[8] dicyandiamide (DCDA),[9] melamine,[10] urea,[11] and thiourea.[12] Although GCN has been extensively employed for a wide range of applications in the fields of energy and sustainability,[13,14] its basic polymerization mechanism has scarcely been investigated and remains unclear. Specifically, depending on the precursor and its C and N content, how the polymerization process changes and the nature of intermediates need to be studied in detail. It has been widely proposed that the thermal condensation of DCDA and CYN proceeds through a sequence of key intermediates like melamine, melam, melem and melon, which eventually form heptazine-based GCN.[15] However, probing how the formation of melamine, which is an important building block and functional unit of GCN, is impacted by precursor type and temperature is essential. Note that the degree of polymerization significantly affects defect formation in GCN and its optoelectronic properties, impacting a range of photoinduced processes such as charge photogeneration and transport and interfacial charge transfer. All these processes crucially impact the solar fuel production efficiency and can be tailored by the rational design of GCN; for this, a comprehensive understanding of the polymerization process plays a key role.

Similar to conducting polymers, π conjugation that is responsible for optical absorption and charge transport in GCN is offered by sp^2-hybridized C and N atoms in the heptazine ring. The highest occupied molecular orbital (HOMO) in

Department of Chemistry, Manipal Institute of Technology, Manipal Academy of Higher Education, Manipal 576104, Karnataka, India.
E-mail: murthy.dharmapura@manipal.edu

GCN consists of N 2p and N 2s orbitals with a minor contribution from C 2p and C 2s orbitals. The lowest unoccupied molecular orbital (LUMO) comprises C 2p and N 2p orbitals.[16] Note that the polymerization process is key for controlling the degree of conjugation, which determines the charge delocalization length, optical absorption onset (the energy difference between π and π* orbitals) and the efficiency of charge transport. However, if the polymerization process is incomplete, unreacted intermediates (condensates) can potentially form N-vacancies that trap photogenerated charge carriers and thereby strongly influence the efficiency of photocatalytic reactions.[17–19] In short, the efficiency of polymerization plays a critical role in extending the conjugation length (and, hence, the optical absorption onset) and in N-vacancy formation, thereby offering an avenue to tailor the optoelectronic properties of GCN and the solar energy conversion efficiency.

Extensive research over the last two decades has focused on the application of GCN in various types of photocatalytic reactions. However, there is no consensus on the thermal polymerization process that leads to the formation of GCN. For example, there is no information available and a lack of consensus on: (i) the chemical nature of the intermediates formed and their thermodynamic properties, (ii) how the polymerization process changes upon employing different precursors with altered C and N amounts, and (iii) whether the thermal polymerization process always involves NH_3 release as a condensation byproduct. Several fundamental questions regarding GCN have been overlooked and need to be addressed. In this direction, we elucidate the polymerization mechanism for the formation of GCN from two widely used precursors—DCDA and CYN. The aim is to provide insights into how changing the precursor will impact the various intermediates formed during the polymerization process and the resulting optoelectronic, surface, photophysical and structural properties. Furthermore, a comprehensive correlation between these properties and the photoelectrochemical (PEC) activity of GCN is rationalised. To the best of our understanding, such a complementary and systematic investigation is the first of its kind, which enables us to offer unique insights into the intriguing polymerization process.

2. Results and discussion

To start with, differences in the structural, surface and optoelectronic properties of GCN synthesized from CYN and DCDA precursors are discussed. GCN samples derived from CYN and DCDA are referred to as GCN-C and GCN-D, respectively. Finally, we rationalize how the polymerization process can follow different pathways depending on the precursor and its impact on the properties and PEC activity.

2.1. Role of changing the precursor on structural, optical and photophysical properties

Fig. 1a presents the XRD patterns of GCN-C and GCN-D. The peak at 27.45° corresponding to the (002) plane with a

d-spacing of 0.324 nm is attributed to the interlayer stacking of heptazine units,[20] whereas the peak from the (100) plane at 13.14° corresponding to a d-spacing of 0.673 nm is ascribed to in-plane repeating heptazine motifs.[21] As shown in Table S1, the peak positions and d-spacing values are similar, indicating that the bulk structural integrity of both synthesized samples remains the same. The chemical functionality of GCN samples was studied using FTIR analysis. Fig. 1b illustrates the FTIR spectra of GCN-D and GCN-C. The peak at 808 cm⁻¹ is ascribed to the characteristic breathing mode of heptazine units, while the peak at 885 cm⁻¹ is attributed to a pattern of cross-linked heptazine deformation.[22] The peaks at 1238, 1319 and 1400 cm⁻¹ are assigned to C–N stretching and the peaks at 1545 and 1631 cm⁻¹ are attributed to C=N stretching of heptazine units. The broad peak at around 3150 cm⁻¹ is characteristic of N–H stretching of –NH/NH₂ groups.[23] Comparing the FTIR spectra indicates a similarity in basic chemical functionality between GCN-D and GCN-C samples.

Fig. 1c shows the optical absorption spectra of GCN-C and GCN-D measured using diffuse reflectance spectroscopy. The similar absorption onset (around 450 nm) for both GCN-C and GCN-D is attributed to the characteristic π-to-π* fundamental transition in GCN. However, GCN-C shows an additional absorption tail, which can be attributed to electron transitions from the HOMO to N-vacancies (which will be discussed later). Fig. S1 presents steady-state photoluminescence (PL) emission spectra of GCN-C and GCN-D. The comparable emission spectra indicate identical radiative recombination phenomena and energetic distributions of emissive states. Fig. 1d compares the tr-PL transients of GCN-C and GCN-D. The similarity in average lifetime (Table S2) and transient decay behaviour indicates that the radiative deactivation mechanism of the photoexcited states in both GCN-C and GCN-D samples is similar.

2.2. Elucidating the precursor-dependent interplay between N-vacancy formation and extended π conjugation

To study changes in the C and N constituents of GCN-C and GCN-D, X-ray photoelectron spectroscopy (XPS) analysis was conducted. Fig. S2 depicts the survey spectra of the synthesized GCN samples, confirming the presence of C, N and O. Fig. 2a and b illustrate high-resolution C 1s core-level XPS spectra. The C 1s spectra were deconvoluted into three peaks at 284.8, 286.8 and 288.3 eV, corresponding to adventitious carbon (Adv. C), C–NH_x (C₁ sites) and N=C–N (C₂ sites), respectively.[24] The peak area percentages and positions remain similar (Table S3) with no significant changes. Fig. 2d compares the valence band XPS (VB-XPS) spectra of GCN-C and GCN-D samples. The absence of a significant shift (<0.05 eV) in the VB onset between the samples indicates that the carrier concentration (indirectly, the Fermi level position within the band gap) does not change. In addition, the similarities of the spectral profiles hint that the distribution of states in both the GCN-C and GCN-D samples is comparable.

To study the electronic nature of N-vacancies in the synthesized samples, N 1s XPS and electron paramagnetic resonance (EPR) analyses were carried out. Fig. 3a and b present
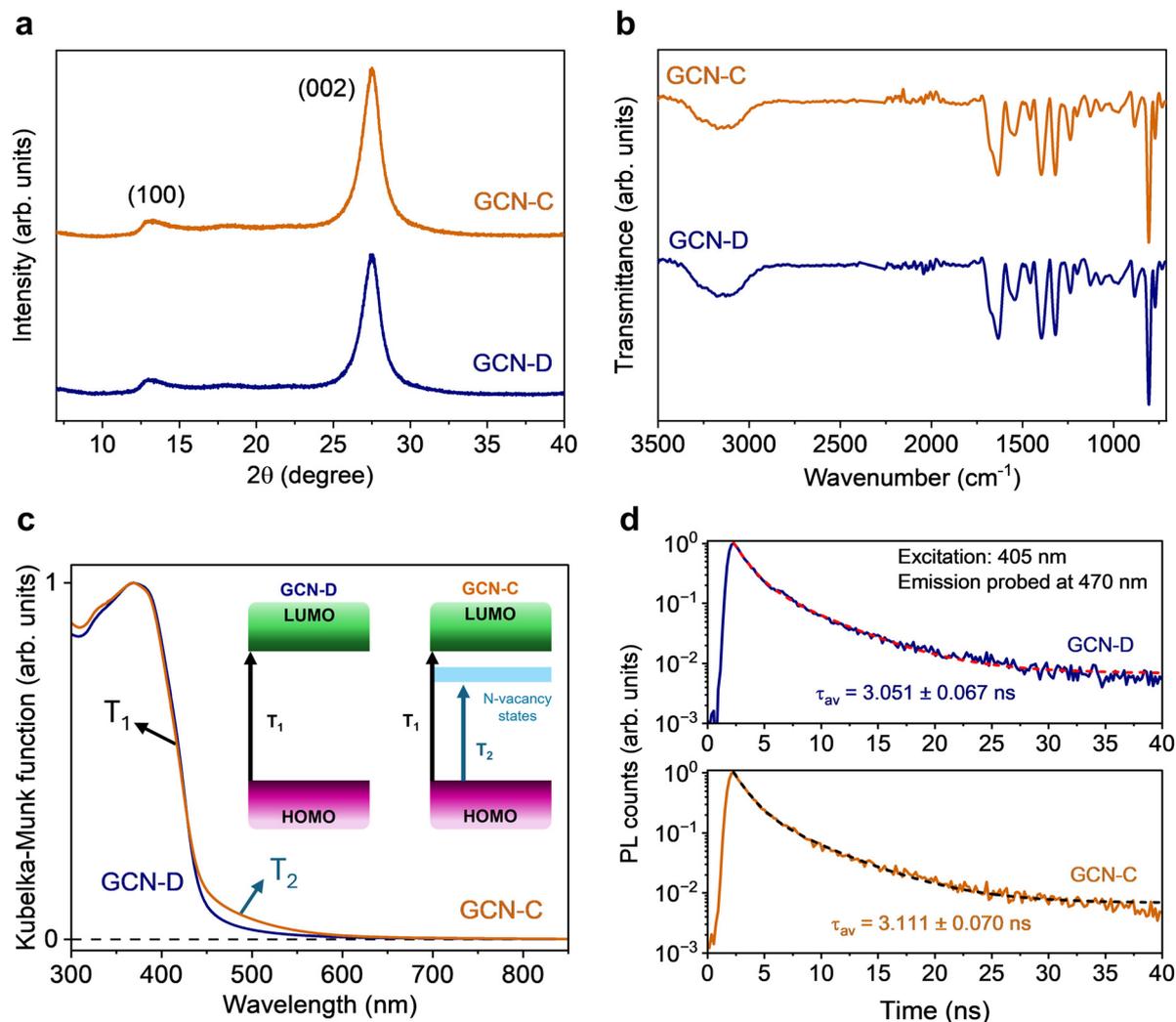
Fig. 1 (a) XRD patterns, (b) FTIR spectra, (c) optical absorption spectra measured in diffuse reflectance mode (inset: electronic transitions), and (d) time-resolved PL (tr-PL) transients of GCN–D and GCN–C. The dotted lines in the transient plots are a result of biexponential function fitting.

the N 1s core-level XPS spectra, which were deconvoluted into three peaks at 398.9, 400.3 and 401.4 eV, ascribed to C=N–C (N_1 sites), N–(C)$_3$ (N_2 sites) and –NH$_x$ (N_3 sites), respectively.[25] The N_1/N_2 peak area ratios from the deconvoluted N 1s spectra elucidate the sites of N-vacancies (either N_1 or N_2 sites). The N_1/N_2 peak area ratios were found to be 3.01 and 5.41 for GCN–C and GCN–D, respectively. A decrease in the ratio proves that N-vacancies are present at N_1 sites in heptazine units. Furthermore, Fig. 2d illustrates the EPR spectra of the synthesized samples. A sharp signal was observed at g = 2.004, which is attributed to unpaired electrons at sp²-hybridized C due to adjacent N-vacancies at two-coordinated nitrogen sites (N_1 sites in Fig. 2c).[26] The higher signal intensity for GCN–C indicates a relatively higher concentration of N-vacancies compared to GCN–D. The N 1s XPS and EPR analyses collectively confirm the presence of a higher concentration of N-vacancies in GCN–C, which also results in the additional optical absorption tail (Fig. 1c).

Table 1 compares the results obtained for GCN–C and GCN–D from all analysis conducted. Despite changing the precursor from CYN to DCDA, which has half the amount of C and N, the bulk of the optoelectronic properties remain virtually similar. One of the most striking observations is the similar optical absorption onset at around 450 nm for both samples. This means that the degree of extended conjugation leads to an energetic difference between π and π* orbitals of around 2.75 eV in both GCN–C and GCN–D. A minor yet significant 12% increase in the N-vacancy concentration for GCN–C is noticed compared to GCN–D. This observation agrees with the pronounced tail-state absorption of GCN–C between 450 and ~560 nm, which is attributed to electron transition from the HOMO to unoccupied N-vacancies below the LUMO (transition T_2 in Fig. 1c). In short, notwithstanding the precursor and C/N content, most of the properties (structural and optoelectronic properties and excited-state behaviour) remain similar. In the following discussion, insights into such intriguing behaviour
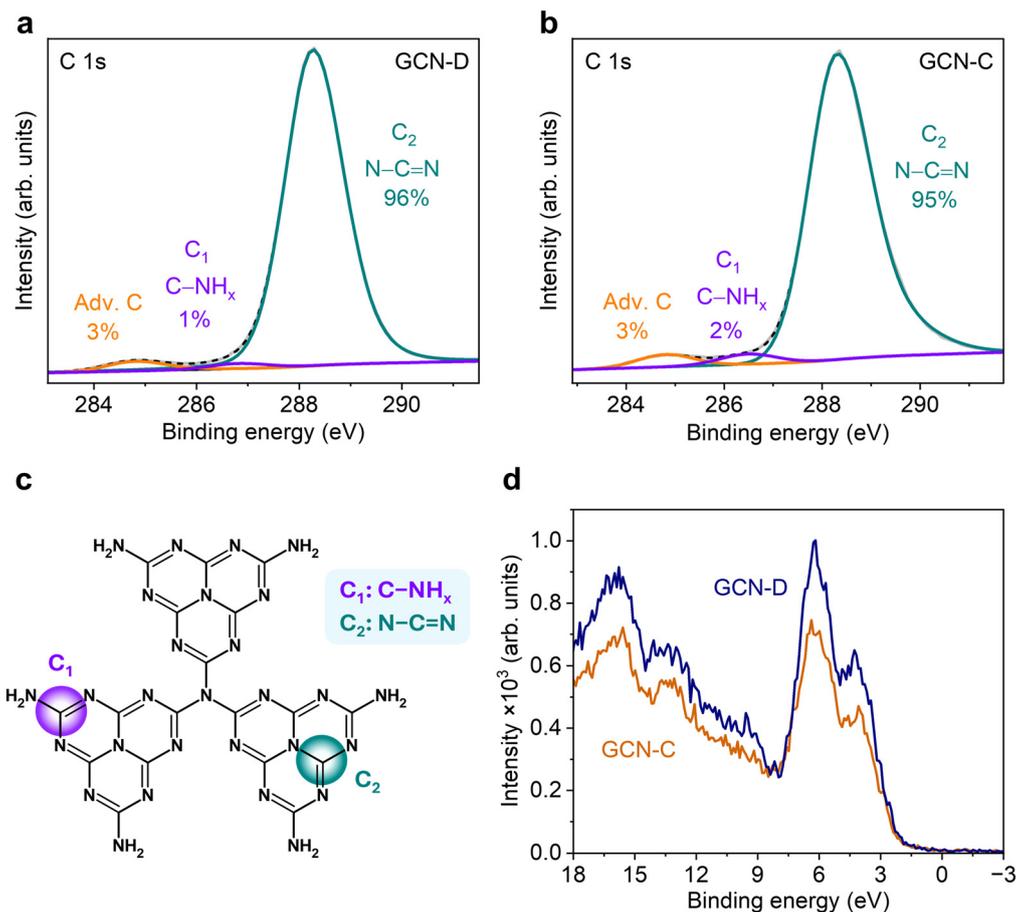
Fig. 2 Deconvoluted high-resolution C 1s core-level XPS spectra of (a) GCN-D and (b) GCN-C. (c) The structure of GCN highlighting C_1 and C_2 sites and (d) VB-XPS spectra of GCN-D and GCN-C.

will be detailed by invoking distinctive polymerization processes that can occur.

2.3. Unveiling precursor-dependent polymerization mechanisms to form GCN

Scheme 1 presents a widely adopted model for the formation of GCN *via* thermal condensation in a stepwise process involving multiple intermediates along with the release of NH_3 as a condensation byproduct.[27,28] Though the formation of GCN from melamine is straightforward, what remains unclear is how melamine is formed from CYN and DCDA precursors. This particular step is often overlooked and not investigated in detail. To answer this question, a detailed and complementary set of experiments was conducted. Differential scanning calorimetry (DSC) and thermogravimetric analysis (TGA) simultaneously offer information on the thermodynamics (exothermic or endothermic) of the polymerization process and on weight loss, respectively. Comparing this data will help to identify the polymerization process in different temperature regions. The unique aspect of this study is monitoring and quantifying the precursor-dependent release of NH_3 (as a condensation byproduct) using temperature-programmed desorp-

tion (NH_3-TPD). Thus, the simultaneous correlation of TGA, DSC and NH_3-TPD data at each temperature can aid in corroborating the polymerization process.

Let us first understand GCN formation from the DCDA precursor, which is now discussed. From DSC analysis of the precursor (Fig. 4a), the endothermic peak for DCDA at 207 °C corresponds to its melting, which is not accompanied by significant weight loss, as deduced from TGA (Fig. 4b). The prominent exothermic peak at 248–262 °C is ascribed to the cyclization of DCDA to form melamine. To confirm this assignment, when pristine melamine was studied using DSC, the exothermic peak at around 250 °C was absent (Fig. S3). Furthermore, the melting of melamine resulted in an endothermic peak at around 328–343 °C. Finally, the condensation of melamine into melem, which requires additional thermal energy, is evidenced by the endothermic peak at 394 °C. Previous studies predicted the release of NH_3 during the polymerization of DCDA,[29] and Fig. 4c shows significant release of NH_3 from DCDA at around 250 °C. As seen in TGA and DSC analysis, the peak at 250 °C is attributed to the formation of melamine. This similarity indicates that DCDA follows a widely adopted polymerization pathway to form mela-
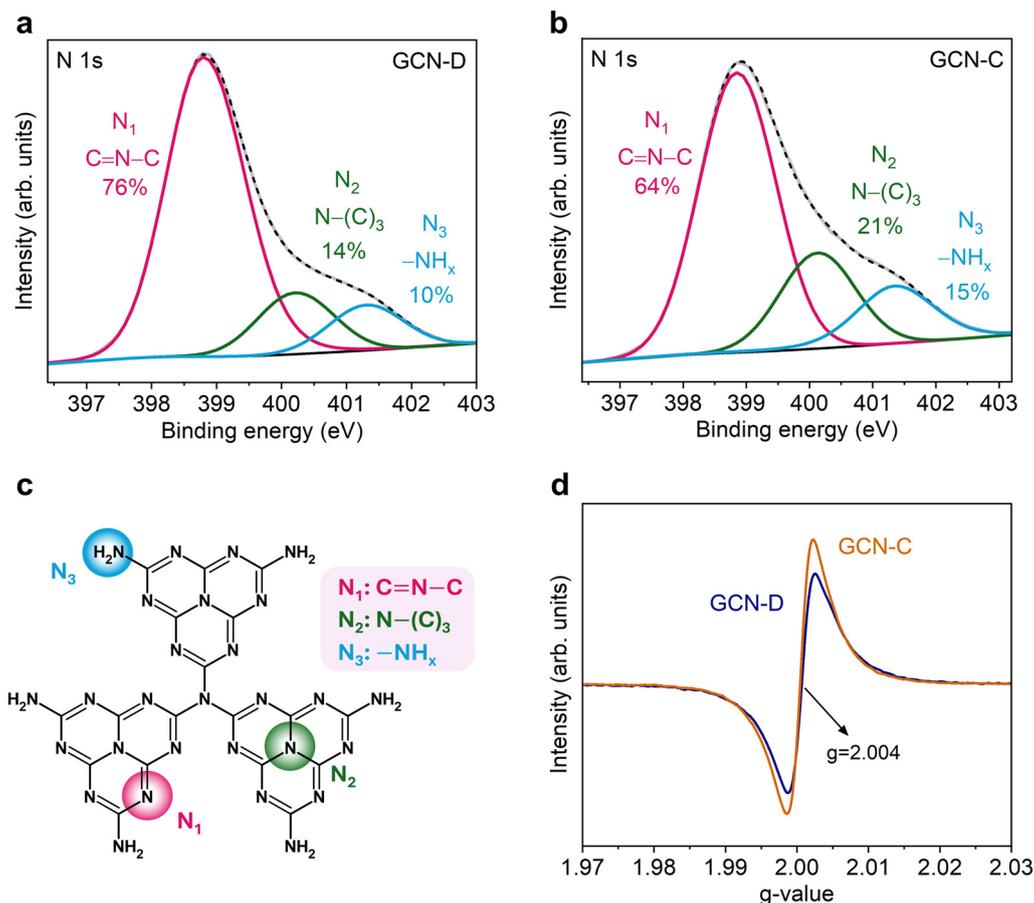
Fig. 3 Deconvoluted high-resolution N 1s core-level XPS spectra of (a) GCN-D and (b) GCN-C. (c) The structure of GCN highlighting N_1, N_2 and N_3 sites and (d) EPR spectra of GCN-D and GCN-C.

Table 1 Summary of experimental observations from GCN-C and GCN-D samples

Similarities noticed	
The bulk structural integrity revealed from XRD	GCN-D ≈ GCN-C
The fundamental π-to-π* energy difference from the optical absorption onset	GCN-D ≈ GCN-C
The photoexcited state decay (lifetime) behaviour from tr-PL analysis	GCN-D ≈ GCN-C
The chemical functionality derived from FTIR	GCN-D ≈ GCN-C
The C constituents estimated from XPS	GCN-D ≈ GCN-C
The valence band onset from XPS	GCN-D ≈ GCN-C

| Differences observed	
The N-vacancy concentration deduced from XPS and EPR	GCN-C > GCN-D
The minor tail-state optical absorption from 450 to ~560 nm	GCN-C > GCN-D

mine with the release of NH_3. Based on these experimental observations, a polymerization mechanism for DCDA is proposed in Fig. 4e. According to this scheme, two molecules of DCDA initially react by nucleophilic attack, further leading to cyclisation and subsequent resonance stabilization to form

melamine at around 248–262 °C. This step will eventually lead to the removal of carbodiimide, which decomposes to release NH_3, as confirmed by NH_3-TPD analysis (Fig. 4c).

GCN formation from the CYN precursor is proposed to occur as follows. The endothermic peak at 44 °C (absent for DCDA) corresponds to the melting of CYN, followed by an exothermic peak between 170 and 174 °C, which is attributed to the dimerization of CYN to form DCDA.[30] This latter process is also found to be accompanied by notable weight loss in the TGA scan (Fig. 4b). Upon the formation of DCDA, similar reactions are followed to form melamine. Comparing the thermal profiles of CYN and DCDA above 248 °C (Fig. 4a and b), similar GCN formation is expected from both precursors once melamine is formed. This observation suggests that melamine serves as the key intermediate and structural building block in the formation of GCN. Interestingly, unlike DCDA, the NH_3-TPD profile of CYN shows that a significantly lower amount of NH_3 is released. This indicates that the polymerization pathway differs in the case of CYN up until the formation of melamine.

Based on this experimental evidence, we propose a detailed mechanism for the formation of melamine from CYN. The lone pair of electrons in the amine group of CYN attacks the electrophilic centre of another adjacent CYN molecule. Further
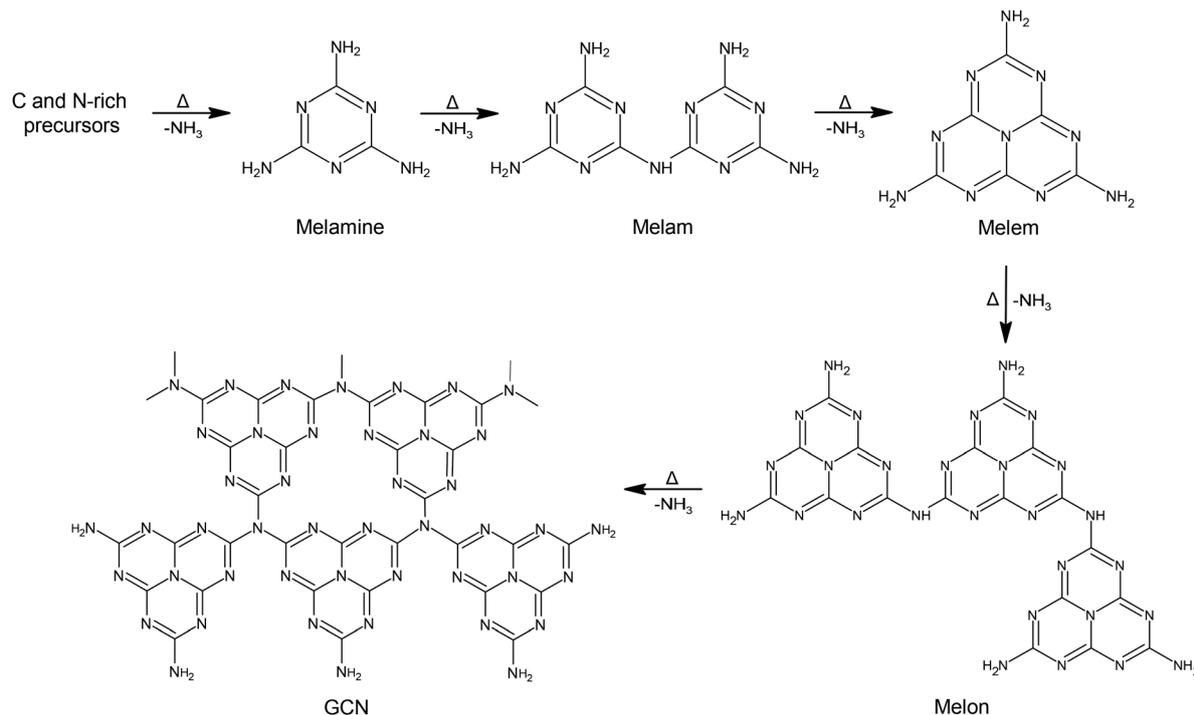
Scheme 1 A generalised polymerization mechanism to form GCN involving an NH$_3$ release model.

rearrangements and tautomerisation lead to the formation of DCDA (170–174 °C). The interaction of DCDA formed at 170–174 °C with other CYN molecules results in further cyclisation, leading to melamine formation. This set of reactions mainly involves rearrangements and thus does not produce significant byproducts, corroborating that a negligible amount of NH$_3$ is released, as confirmed by NH$_3$-TPD analysis.

2.4. Interplay between N-vacancies, extended π conjugation, the polymerization process and PEC activity

As shown in Fig. 3, both XPS and EPR data confirmed that GCN-C has ~10% more N-vacancies than GCN-D. With this information, we now aim to establish a plausible correlation between N-vacancy formation and the precursor-dependent polymerization process. Fig. 4b shows 25% weight loss for CYN during TGA in conjunction with a pronounced exothermic reaction, attributed to the dimerization of CYN to form DCDA. However, the proposed dimerization mechanism of CYN (Fig. 4f) is not expected to involve the release of NH$_3$ or the loss of any C or N constituent atoms. This discrepancy suggests that some of the CYN precursor undergoes partial (self) decomposition to release NH$_3$ (Fig. 4c, around 170 to 174 °C) and thereby forms intermediate condensates, potentially influencing the optoelectronic properties. The weak tail-state optical absorption due to T$_2$ transitions (Fig. 1c) observed only for GCN-C further validates the role of incomplete condensates in affecting in-gap unoccupied N-vacancy formation. Though the experimental data strongly point towards our proposed model discussed earlier, further experiments are necessary to understand this intriguing phenomenon.

It is essential to understand the effect of the yield of GCN upon changing the precursor when commenting on the optoelectronic properties. The GCN yields obtained from CYN and DCDA precursors were found to be 42.6 and 50.8%, respectively. For both GCN-C and GCN-D, the fundamental π-to-π* transition at ~450 nm is unaltered. This means that despite differences in the GCN yield and CYN having half the amount of C/N compared to DCDA, a minimum number of melamine units subsequently polymerized to form electronically connected functional heptazine units to endow the materials with a sufficient π-conjugation length. Thus, preserving the C and N content and not allowing the release of NH$_3$ seems to be key for obtaining a virtually similar π-to-π* transition at ~450 nm and functionality in GCN.

In our earlier discussion, the optoelectronic properties of GCN samples derived from both precursors were found to be virtually similar. To further evaluate these observations, the PEC performances of GCN-C and GCN-D are compared. Fig. 5a shows the CV data from GCN-D and GCN-C. Both samples exhibit similar CV profiles, with a higher current response on the cathodic side compared to the anodic side, demonstrating their potential for the H$_2$ evolution reaction in agreement with earlier reports.[31] To confirm the cathodic behaviour, i.e., that electrons are indeed the active species, CV experiments were conducted in the presence of H$_2$O$_2$, as depicted in Fig. 5b. The threefold enhancement in the cathodic current corroborates the notion that electrons are indeed involved in the probed electrochemical reaction. Fig. 5c and d show increment in photocathodic current by a factor of 1.23 and 1.09 for GCN-D and GCN-C samples, respectively. The electrochemically active
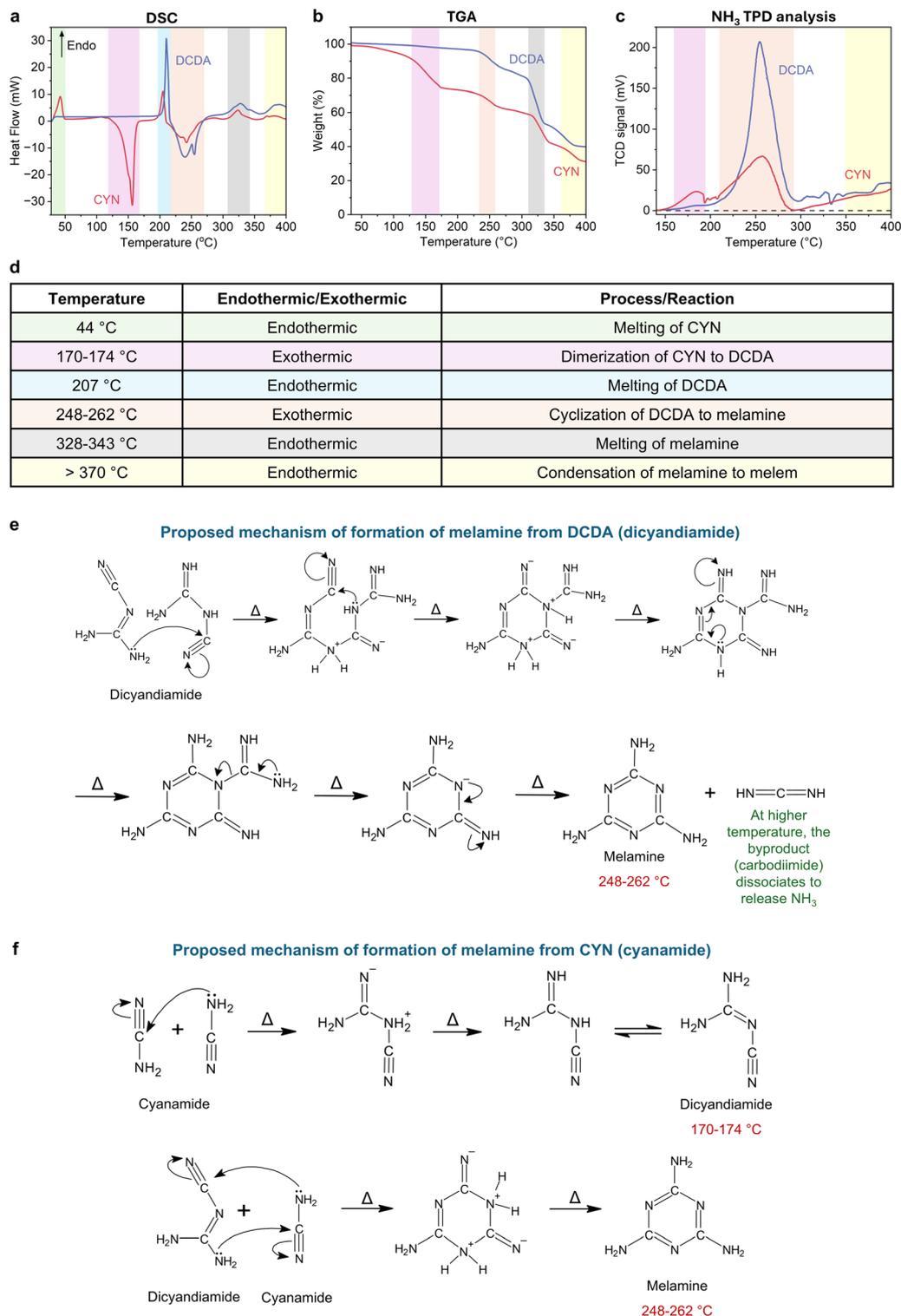
Fig. 4 (a) DSC thermograms, (b) TGA thermograms and (c) NH$_3$–TPD profiles of the DCDA and CYN precursors. (d) The processes/reactions involved in thermal polymerization to form GCN using DCDA and CYN. Schematic diagrams demonstrating the proposed formation of melamine from (e) DCDA and (f) CYN.

surface areas (ECSAs) of GCN-D and GCN-C are 1.20 and 1.29 cm^2 (Fig. S4), respectively. This suggests that both samples have similar ECSAs. However, the magnitude of the photocathodic current of GCN-D is slightly higher compared to GCN-C, which may indirectly be attributed to an increased concentration of in-gap unoccupied N-vacancies that can
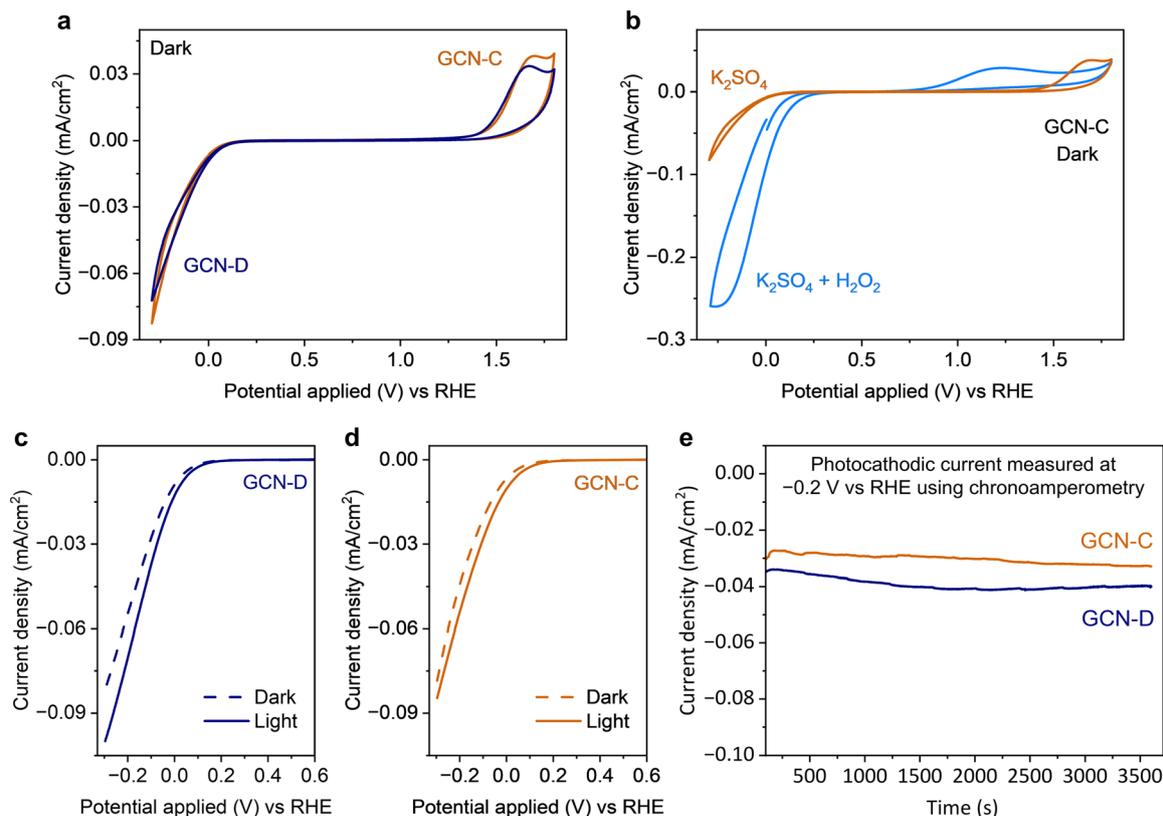
Fig. 5 (a) Cyclic voltammetry (CV) data from GCN-D and GCN-C. (b) A comparison of CV data from GCN-C in the presence and absence of 0.3 mM H_2O_2 as an electron acceptor. Linear sweep voltammetry (LSV) data from (c) GCN-D and (d) GCN-C under dark and light irradiation ($\lambda > 420$ nm) conditions. All CV and LSV data are iR corrected. (e) Chronoamperometry measurements performed at −0.2 V *vs.* RHE. Reaction conditions: AM 1.5 G; power density = 1000 W m^{-2}; pH = 5.6; scan rate = 50 mV s^{-1}.

potentially trap photogenerated electrons, leading to their inefficient migration towards the interface, thereby causing a marginal reduction in the photocathodic current of GCN-C compared to GCN-D. The chronoamperometry measurements shown in Fig. 5e indicate the prolonged stability of both these photoelectrodes measured up to one hour under light and bias. From a collective comparison of the data in Fig. 5, it is essential to note that both GCN-C and GCN-D, despite being formed from two different precursors *via* distinct polymerization mechanisms and notwithstanding the amount of NH_3 released, demonstrate comparable PEC performances.

Though the polymerization mechanism presented here is related to heptazine-based GCN, a similar model may well be applicable in other classes of carbon nitrides, such as poly(heptazine imides) (PHIs) and poly(triazine imides) (PTIs). These newly emerging families of 2D photocatalysts based on C and N have attracted significant attention for overall water splitting,[32] CO_2 reduction,[33] NH_3 production[34] and H_2O_2 production.[35] These systems feature a delocalized π-electron system with triazine or heptazine units linked by imide groups and often require the use of eutectic salt melts with precursors to realize high performance.[36] However, it is unclear how polymerization happens in these systems, which significantly impacts the photocatalytic performance. The new approach

presented here may also be applied to elucidate correlations between polymerization mechanisms and photocatalytic activity. Such insights are essential when designing these materials to enhance the solar-to-chemical energy conversion efficiencies of these promising low-cost photocatalysts.

3. Conclusions

Despite the extensive utilization of GCN in photocatalytic reactions for sustainable applications and solar energy conversion, there is an inadequate understanding of how GCN is formed *via* thermal polymerization. Intrigued by this question, we systematically unveil the polymerization process using complementary thermal and NH_3-TPD analyses for the first time and correlate our data with the observed optoelectronic/structural/surface properties. Such a comprehensive investigation demonstrated that the thermal polymerization process to form GCN need not always release NH_3 as a condensation byproduct. Overall, this work provides critical insights into the distinctive reaction pathways that form melamine building blocks *via* the polymerization of DCDA and CYN precursors. Correlating N-vacancy formation and the optoelectronic properties of GCN with the polymerization process and PEC

activity offered unique rational insights into tailoring the opto-electronic properties of GCN. These results may encourage further investigations, particularly those that have previously ignored the polymerization process, to gain a deeper understanding and thereby enhance the solar energy conversion efficiencies of these promising and cost-effective polymer-based photocatalysts.

4. Experimental section

4.1. Synthesis of GCN-D and GCN-C

Dicyandiamide (98%, Loba Chemie) and cyanamide (99%, Sigma-Aldrich) were used for synthesis without any further treatment. GCN was synthesized by heating DCDA at 550 °C for 3 h and is named GCN-D. GCN-C was also synthesized in a similar procedure using CYN as the precursor. To allow a comparison, the heating rate and duration were kept similar for both precursors.

4.2. Structural, surface and optoelectronic characterization tools

Powder XRD data were recorded using a Rigaku SmartLab diffractometer with Cu-Kα radiation as the radiation source, with a wavelength (λ) of 1.5406 Å. The sample was mounted on the sample holder, and the XRD pattern was recorded at a scan speed of 2.00° min^{-1} with a 0.01° step width. FTIR spectroscopy was performed with a Shimadzu IRSpirit spectrophotometer in ATR mode. The optical absorption spectra of the synthesized samples were measured using a JASCO V-770 UV/Vis/NIR spectrometer equipped with an integrating sphere in diffuse reflectance mode. The steady-state PL measurements were carried out using an Edinburgh Instruments FLS1000 photoluminescence spectrometer. A 450-W ozone-free xenon arc lamp was used as the light source. For tr-PL measurements, the time-correlated single photon counting (TCSPC) technique was used. A picosecond pulsed diode laser of 405 nm was used as an excitation source, and a visible photomultiplier tube (PMT) was used as a detector. XPS analysis was carried out using a Thermo Scientific K-Alpha X-ray photoelectron spectrometer. Spectral charge correction was performed based on the C 1s peak appearing at 284.8 eV. EPR spectra were analyzed using a JEOL Model JES FA200 spectrometer. DSC measurements were conducted using a PerkinElmer DSC 6000 instrument. Equal amounts of precursor mixture were heated at a ramp rate of 5 °C min^{-1} under argon atmosphere. TGA analysis was conducted using a PerkinElmer STA 6000 thermal analyzer. NH$_3$-TPD analysis was carried out using the Autosorb 6200 EPDM XR instrument. The samples were heated at a ramp rate of 10 °C min^{-1}, and the NH$_3$ released was quantified. The amounts of sample taken for analysis were as follows: DCDA = 0.020 g, CYN = 0.220 g.

4.3. Photoelectrochemical measurements

The working electrodes for PEC measurements were prepared as follows. 100 mg of photocatalyst (GCN-D and GCN-C) and 20 mg of ethyl cellulose were ground for 10 min. This mixture was then added to a solution containing 1 mL of ethanol and 20 μL of Nafion. The solution was sonicated for 2 h, followed by stirring it overnight to prepare a photocatalyst ink. 50 μL of the prepared ink was spin-coated on ITO (indium tin oxide)-coated glass substrates. The electrodes were then calcined at 300 °C for 2 h. The PEC measurements were carried out using a potentiostat (Metrohm Autolab PGSTAT 204) and a solar simulator (Holmarc HR-SS300WRM1-100A) equipped with an air mass (AM 1.5 G) filter, and a 300-W xenon short arc lamp with a 420 nm long pass filter was used as the light source. A three-electrode system, with the ITO-coated glass substrate as the working electrode and a platinum and reversible hydrogen electrode (RHE) as the counter and reference electrodes, respectively, was used for the measurements. 0.1 M K$_2$SO$_4$ (pH 5.6) was used as the electrolyte. CV scans were recorded over a potential range of −0.3 V to 1.8 V *vs.* RHE at a scan rate of 50 mV s^{-1}. LSV analysis was performed from 0.8 V to −0.3 V *vs.* RHE at a scan rate of 50 mV s^{-1}. The reported CV and LSV data involve iR-corrected potential values. The stability of the electrodes was studied using chronoamperometry measurements at −0.2 V *vs.* RHE for 1 hour. The ECSA was calculated by recording CV scans in the non-faradaic region at scan rates ranging from 10 mV s^{-1} to 50 mV s^{-1}. The double-layer capacitance (C_{dl}) was obtained from a plot of anodic current (j_a)–cathodic current (j_c) *vs.* the scan rate at a given potential. The ECSA was calculated using C_{dl}/C_s, where C_s is the specific capacitance of GCN.

Author contributions

S. J. G. conducted the synthesis, structural/surface/optoelectronic characterization of the materials and analysis. S. J. G. and D. H. K. M. wrote the first version of the article. S. S. M. conducted thermal analysis measurements of the materials. S. S. M. and S. R. K. conducted the PEC measurements. S. R. K. deduced the polymerization mechanism. D. H. K. M. conceptualized the work, interpreted the results, edited the article, and coordinated the overall work. The article was written through contributions from all authors.

Conflicts of interest

The authors declare no conflict of interest.

Data availability

The data supporting this article have been included as part of the manuscript and supplementary information (SI). Supplementary information: XRD peak positions and calculated *d*-spacing values, steady-state PL emission spectra, PL lifetimes obtained from fitting, survey spectra from XPS, XPS peak parameters from the deconvolution of C and N 1s core-level spectra, and the DSC thermogram of melamine. See DOI: https://doi.org/10.1039/d5py01003a.

Acknowledgements

References

1 W. J. Ong, L. L. Tan, Y. H. Ng, S. T. Yong and S. P. Chai, *Chem. Rev.*, 2016, **116**, 7159–7329.

2 R. Han, Y. Wang, Z. Liu and J. Wang, *ACS Appl. Energy Mater.*, 2025, **8**, 883–893.

3 Y. Han, M. Liu, A. Sun, F. Zhao, J. Zhao and C. A. Wang, *Polym. Chem.*, 2025, **16**, 1603–1612.

4 L. Hu, J. Yu, Y. You, G. Zhou, M. Yuan, N. Wu, L. Zhao and Z. Jiang, *New J. Chem.*, 2025, **49**, 12585–12593.

5 J. Yingsu, Y. Liu, H. Huang, L. Yang, Y. Qian, X. Fu and H. Liu, *J. Phys. Chem. C*, 2023, **127**, 8687–8694.

6 V. G. Merkulov, O. V. Turova, E. A. Ivanova, I. V. Kuchurov, M. N. Zharkov and S. G. Zlotin, *ChemPhotoChem*, 2025, **9**, e202400227.

7 Z. G. Coban, C. Esen, B. Kumru, A. Kocaarslan, Y. Yagci and B. Kiskan, *Macromolecules*, 2024, **57**, 4508–4515.

8 Z. Sun, J. Lin, K. Hou, L. Guan and H. Zhan, *J. Mater. Chem. A*, 2020, **8**, 7273–7279.

9 R. M. Yadav, R. Kumar, A. Aliyan, P. S. Dobal, S. Biradar, R. Vajtai, D. P. Singh, A. A. Martí and P. M. Ajayan, *New J. Chem.*, 2020, **44**, 2644–2651.

10 L. Wang, Y. Hou, S. Xiao, F. Bi, L. Zhao, Y. Li, X. Zhang, G. Gai and X. Dong, *RSC Adv.*, 2019, **9**, 39304–39314.

11 F. Safari, R. Poursalehi and H. Delavari, *RSC Adv.*, 2024, **14**, 26943–26953.

12 H. Chand, A. Kumar, S. Goswami and V. Krishnan, *Fuel*, 2024, **357**, 129757.

13 X. Yang, J. Peng, L. Zhao, H. Zhang, J. Li, P. Yu, Y. Fan, J. Wang, H. Liu and S. Dou, *Carbon Energy*, 2024, **6**, e490.

14 D. Bhanderi, P. Lakhani and C. K. Modi, *RSC Sustainability*, 2024, **2**, 265–287.

15 P. Sharma, P. P. Sarngan, A. Lakshmanan and D. Sarkar, *J. Mater. Sci.: Mater. Electron.*, 2022, **33**, 9116–9125.

16 Y. Chen, B. Wang, S. Lin, Y. Zhang and X. Wang, *J. Phys. Chem. C*, 2014, **118**, 29981–29989.

17 S. Chandrappa, S. J. Galbao, A. Furube and D. H. K. Murthy, *ACS Appl. Nano Mater.*, 2023, **6**, 19551–19572.

18 T. Liu, W. Zhu, N. Wang, K. Zhang, X. Wen, Y. Xing and Y. Li, *Adv. Sci.*, 2023, **10**, 2302503.

19 Y. Liang, L. Wu, L. Zeng and Y. Jiang, *Polym. Chem.*, 2025, **16**, 4356–4363.

20 T. Alizadeh, S. Nayeri and N. Hamidi, *RSC Adv.*, 2019, **9**, 13096–13103.

21 T. Xiong, W. Cen, Y. Zhang and F. Dong, *ACS Catal.*, 2016, **6**, 2462–2472.

22 A. Olufemi Oluwole, P. Khoza and O. S. Olatunji, *ChemistrySelect*, 2022, **7**, e202203601.

23 S. Samanta, S. Martha and K. Parida, *ChemCatChem*, 2014, **6**, 1453–1462.

24 J. R. Zhang, Y. Ma, S. Y. Wang, J. Ding, B. Gao, E. Kan and W. Hua, *Phys. Chem. Chem. Phys.*, 2019, **21**, 22819–22830.

25 C. Zhao, C. Ding, C. Han, X. Yang and J. Xu, *Sol. RRL*, 2021, **5**, 2000486.

26 C. Lv, Y. Qian, C. Yan, Y. Ding, Y. Liu, G. Chen and G. Yu, *Angew. Chem.*, 2018, **130**, 10403–10407.

27 M. J. Bojdys, J. O. Müller, M. Antonietti and A. Thomas, *Chem. – Eur. J.*, 2008, **14**, 8177–8182.

28 B. Jürgens, E. Irran, J. Senker, P. Kroll, H. Müller and W. Schnick, *J. Am. Chem. Soc.*, 2003, **125**, 10288–10300.

29 H. Bieling, M. Radüchel, G. Wenzel and H. Beyer, *J. Prakt. Chem.*, 1965, **28**, 325–340.

30 M. Cao, K. Wang, I. Tudela and X. Fan, *Appl. Surf. Sci.*, 2020, **533**, 147429.

31 Q. Zhu and J. Zhang, *Environ. Funct. Mater.*, 2022, **1**, 121–125.

32 X. Li, X. Chen, Y. Fang, W. Lin, Y. Hou, M. Anpo, X. Fu and X. Wang, *Chem. Sci.*, 2022, **13**, 7541–7551.

33 B. Su, S. Wang, W. Xing, K. Liu, S. F. Hung, X. Chen, Y. Fang, G. Zhang, H. Zhang and X. Wang, *Angew. Chem., Int. Ed.*, 2025, **64**, e202505453.

34 S. F. Blaskievicz, I. Freitas Teixeira, L. H. Mascaro and J. Ferreira de Brito, *ChemCatChem*, 2023, **15**, e202201610.

35 J. Bharti, J. Odutola, Z. Hajiahmadi, K. Nolkemper, Z. Tian, H. Tong, V. Shvalagin, T. D. Kühne, T. P. Ruoko and C. M. Pelicano, *Adv. Mater.*, 2025, e10585.

36 C. M. Pelicano and M. Antonietti, *Angew. Chem., Int. Ed.*, 2024, **63**, e202406290.